Computers in Biology and Medicine 108 (2019) 174–181

Contents lists available at ScienceDirect

Computers in Biology and Medicine

journal homepage: www.elsevier.com/locate/compbiomed

A two-step risk assessment method for radiofrequency ablations of spine metastases

N. Merten[a,b,*], S. Adler[c,b], G. Hille[a,b], M. Hanses[c,b], M. Becker[d], S. Saalfeld[a,b], B. Preim[a,b]

[a] Otto-von-Guericke University, Department of Simulation and Graphics, Universitätsplatz 2, D-39106, Magdeburg, Germany
[b] Research Campus STIMULATE, Sandtorstraße 23, D-39106, Magdeburg, Germany
[c] Fraunhofer IFF, Sandtorstraße 22, D-39106, Magdeburg, Germany
[d] University Hospital Magdeburg, University Clinic for Neuroradiology, Leipziger Str. 44, D-39120, Magdeburg, Germany

ARTICLE INFO

Keywords:
radiofrequency ablations
Needle-based interventions
Risk visualization
Bone drilling
Treatment of bone metastases

ABSTRACT

Background: Spine metastases (MTS) can be treated via Radiofrequency Ablation (RFA) electrodes. To bring these electrodes into vertebral MTS, pathways have to be created. This can be done via transpedicular hammering or drilling. However, this is challenging due to spatial constraints, and because MTS can alter bone density considerably.

Method: In this work a two-step method is presented that intends to offer cognitive and physical assistance. *Step 1* comprises two visualization methods that depict safety margins between and in risk structures. For *Step 2*, the correlation between Hounsfield Units (HUs) and drilling forces was analyzed to support manual and robot-assisted RFAs.

Results: In-depth descriptions of two clinical cases and detailed feedback from the local clinic of neuroradiology are used to present the capabilities of the proposed method. Furthermore, a stiffness criterion is presented to predict drilling force changes from the local distribution and homogeneity of HUs with an inaccuracy of less than 1 mm.

Conclusions: The combination of visualization and drilling force prediction shows potential to support manual and robot-assisted spine RFAs. However, limitations have to be addressed in the future. For example, it has to be carefully evaluated to which extent the proposed method can speed up the planning process and increase intervention safety.

1. Introduction

Bone health is maintained due to a well-balanced communication and interaction between various bone tissue cells. Two of their main functions are synthesizing new and breaking down old bone tissue. Cancer cells can cause communication imbalances, which, in turn, can result in *ossificating* or *ostelytic* bone diseases: The former term is used for the pathological process of bone hardening, whereas the latter describes an excessive amount of bone tissue resorption. This results in loss of structural integrity and pain.

The most frequently conducted bone metastases treatments are radiotherapy, chemotherapy, surgery, or combinations of them [1]. *Radiofrequency Ablations* (RFAs) are an image-guided intervention that can reduce bone pain [2]. The location and size of metastases determine if and how RFAs are implemented. If feasible, first, pathways into affected vertebrae have to be created, for example, by hammering cannulated trocars or drilling through their pedicles. Pedicles are the circular-shaped bony structures that encompass the spinal canal laterally. After pathways are created, RFA electrodes are inserted to coagulate surrounding tissue.

A simplified version of the current clinical workflow at the University Hospital of Magdeburg is depicted in the top row of Fig. 1. For diagnosis and intervention planning, multiple *Magnetic Resonance Imaging* (MRI) sequences (T1 with and without contrast agent, T2, and Short Tau Inversion Recovery) and a *Computed Tomography* (CT) scan are recorded. This combination is necessary to select a feasible therapy: Whereas cancerous bone tissue can remain totally occult in CT, it can be detected in MR image data [9]. Furthermore, the contrast-enhanced MRI scans depict the vascularization inside vertebrae, which is an important feature to conclude about the primary cancer's origin. In

* Corresponding author. Otto-von-Guericke University, Department of Simulation and Graphics, Universitätsplatz 2, D-39106, Magdeburg, Germany.
E-mail addresses: nmerten@isg.cs.uni-magdeburg.de (N. Merten), simon.adler@iff.fraunhofer.de (S. Adler), georg@isg.cs.uni-magdeburg.de (G. Hille), magnus.hanses@iff.fraunhofer.de (M. Hanses), mathias.becker@med.ovgu.de (M. Becker), sylvia@isg.cs.uni-magdeburg.de (S. Saalfeld), preim@isg.cs.uni-magdeburg.de (B. Preim).

https://doi.org/10.1016/j.compbiomed.2019.03.007
Received 16 January 2019; Received in revised form 8 March 2019; Accepted 9 March 2019
0010-4825/

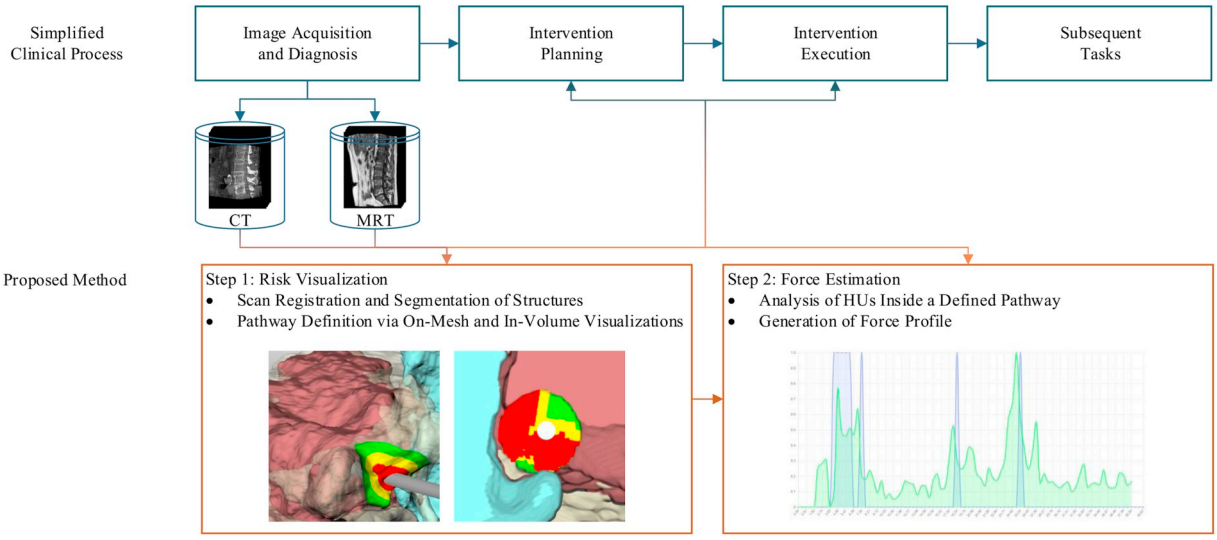

Fig. 1. The currently implemented clinical workflow (top row) and the proposed two-step method (bottom row). For *Step 1*, first, an image registration between the MRI and CT scans is performed. Subsequently, segmentation masks of the spinal canal (blue), the metastasis (red), and remaining bone tissue of the affected vertebra (brown) are obtained. These masks are then used for the *on-mesh* and *in-volume* visualization methods to define a low risk pathway into the vertebra and metastasis. For *Step 2*, the Hounsfield Units along this pathway are then used to estimate drilling forces. This estimation could then be used to validate a drill's position during robot-assisted interventions.

contrast, CT scans are required to reliably conclude about the density of osseous structures.

Hammering and drilling through pedicles are challenging tasks, because force and accuracy have to be balanced: On the one hand, enough force has to be applied to penetrate bone tissue. On the other hand, nearby risk structures, such as the spinal canal, must not be injured. Furthermore, instruments must not pierce vertebrae in ventral direction, which could injure the lungs or abdominal aorta. Spine RFAs are also spatially challenging, because the diameter of lumbar pedicles ranges from 5 mm to 8 mm and for thoracic pedicles from 3 mm to 4 mm, respectively.

For instrument placement during interventions, DynaCT scans are acquired. These scans take 20 s and are performed under apnea to eliminate breathing artifacts. After pathway creation, the insertion depth and final instrument placement are validated with an additional DynaCT scan. Then, the ablation is performed. Afterwards, a vertebroplasty or kyphoplasty can optionally be conducted to restore structural integrity.

In this work, a two-step method is proposed that is intended to improve the planning and execution of spine RFAs (cf. Fig. 1). The main goal of *Step 1* is to offer cognitive support via 3D visualizations. During pathway definition and instrument insertion, the on-mesh and in-volume visualization methods depict safety margins to risk structures, such as the spinal canal, and the insertion depth.When a pathway is defined, the stiffness criterion ρ of *Step 2* is used to analyze the local distribution and homogeneity of Hounsfield Units (HUs) (see Fig. 6). Thus, areas with very dense or porous bone tissue are utilized to provide an estimation of how much force is required to further advance an inserted instrument. These information are important to choose a low-risk pathway, and to validate the instrument's position during interventions.

In Section 2 and 3, related work and our method is described, respectively. Results and detailed feedback from the local division of neuroradiology are presented in Section 4 and 5. Results and open questions are discussed in Section 6 and 7.

2. Related work

Needle-based interventions, such as biopsies and RFAs, always pose a *risk*. Here, risk usually is a combination of various *Risk Aspects*, and aspects that were repeatedly used in related work are.

- Safety Margins to nearby risk structures,
- the Pathway Length between entry and target point,
- the Instrument's Diameter,
- the Insertion Angle, relative to a context structure's surface,
- and the Ablation Zone that was or will be created.

Table 1 shows related visualization methods and, depending on the implementation, they were assigned to one of three categories: Risk can either be presented on a surface mesh, through an outward projection, or by using an additional, map-like presentation. Generally, the

Table 1
Combinations of risk aspects and related visualization methods. Parenthesized cross marks indicate that respective aspects were discussed or considered for future work, but were not yet implemented.

		Risk Aspects					Risk Coding
Category	Citation	*Safety Margin*	*Pathway Length*	*Instrument Diameter*	*Angle*	*Ablation Zone*	low → high
Mesh	Baegert et al. <3>	×	×		(×)	×	
	Zombori et al. <4>	×	×		×		
Projection	Navkar et al. <5>	×	×	×			
	Rincón-Nigro et al. <6>	×	×				
Map	Herghelegiu et al. <7>	×		×	(×)		
	Rieder et al. <8>	×				×	
Mesh & Volume	Proposed method	×	(×)	×			

methods listed use weighting functions to quantify risk, which is then used for color-coding. Butz et al. [10] did pioneering work in computer-assisted planning of tumor ablations incorporating image analysis and simulation of treatment effects. Later, Littmann et al. [11] implemented a system that also considered simulation to assess cooling effects during ablations. Moreover, they showed how to plan an access path with a combination of 2D slice-based, 3D overview, and 3D detail visualizations.

Baegert et al. [3] use a sequential brightness scale to visualize risk on skin meshes for ablations of hepatic metastases. Zombori et al. [4] also use a mesh-based method to show pathway risk on skull meshes for Stereo Electroencephalographies using a sequential, green-to-red color scale. Rincón-Nigro et al.'s [6] work is a GPU-accelerated version of Navkar et al.'s [5] projection-based method. Additionally, the updated version uses a diverging blue-white-red color scale, whereas the original method used a qualitative yellow-red color scale.

These methods depict risk on meshes. However, they were separated into two categories, because the processing of safety margins, which is a crucial risk aspect, and visualization of high risk pathways are different. For both types of methods, a target point, e. g., inside a lesion, is defined. Subsequently, for each pathway, i. e., virtual lines between a target point and all surface mesh vertices, it is assessed if they undershoot a user-defined safety margin to risk structures, such as blood vessels. One possibility is to sample each pathway in equidistant steps and compute the absolute minimum distance between each sample point and risk structures, which is realized by the presented mesh-based methods. Projection-based methods, related to ray casting, search for intersections between pathways and risk structure geometry. If this is the Case, unfeasible pathways are assigned a unique color-coding on the surface mesh, e. g., black. In contrast, the presented mesh-based methods visually omit unfeasible pathways, e. g., by rendering them transparent.

Regarding map-like methods, Herghelegiu et al. [7] use a sequential, green-to-red color scale in a 2D layout to assist brain biopsies of deep-seated tumors. The authors also discuss other clinical procedures, such as neurosurgical keyhole interventions. In the context of using additional, map-like risk visualizations, the method of Rieder et al. [8] is special: First, it was not used to convey pathway risk, but to color-code coagulation zones after liver tumor ablations. Secondly, the authors utilized the *Mollweide Projection*, which is a projection technique typically used to create 2D maps of the globe, to transform 3D coagulation zones into 2D maps using a qualitative green-yellow-red color scale.

The first contribution of the proposed method is the combination of safety margins, pathway length, and the instrument diameter to define risk. For needle-based interventions in the brain or liver, for which the pathway length is minimized, the risk of breaking through target anatomy to injure subsequent structures is rather low [3,5]. If, after careful consideration, longer pathways are deemed feasible, this aspect could be addressed by entering the organ from a different surface area. For vertebrae this is challenging due to strict spatial constraints, e. g. because of their small pedicles, and the necessity to penetrate the corticalis as perpendicular as possible to prevent bone chipping or comminution. Moreover, instruments have to be inserted into metastases, which can bring them very close to the front side of targeted vertebrae. These aspects are addressed by the proposed method and the qualitative color-coding, which supports the process of distinct, clinical decision making. However, if a binary color-coding is necessary, the transfer functions from Fig. 2 can be adapted accordingly.

For the second contribution, it is presented how HUs and drilling forces relate to each other in dried and fat-freed human bones. Drilling and hammering are unique tasks to bring instruments into bones and are not needed for more soft anatomical structures, such as the brain or liver. Moreover, metastases can heavily alter bone density. Thus, a priori knowledge about varying bone tissue density along the insertion path is important. We can show that drilling force changes depend on the variety of bone tissue densities in a larger radius around the drilling path. However, note that although this criterion allows for accurate drilling force predictions, it is the result of observations alone and further research is required. The final contribution is a detailed description of the capabilities and limitation of the proposed two-step method and how it could be included in clinical workflows to improve the planning and execution processes of spine RFAs in the future.

3. Two-step visual risk communication

In this section, the proposed two-step method is described in detail (cf. Fig. 1). For *Step 1*, the processing pipeline for the *in-volume* and *on-mesh* visualization methods will be explained. For *Step 2*, bone drilling experiments were conducted and thus, the experimental drilling setup is described (see Fig. 3). The methods were implemented using *MeVisLab 2.8.2* [12].

3.1. Step 1 – risk visualization

In our previous work, a combined projection-based and map-like approach was presented [13]. However, we decided to use a combination of mesh-based and volume-based visualization approaches (cf. Table 1): First, this combination does not require the use of an additional 2D view, which is generally necessary for map-like methods. Secondly, a volume-based approach enables a visual encoding of safety margins in all spatial directions simultaneously. In contrast, one main advantage of projection-based techniques is the easy-to-understand approach to test and visualize intersections between pathways and inlying risk structure geometry. However, in the presented clinical context, inlying risk structures do not have to be considered.

The on-mesh and in-volume methods require that the remaining vertebra, the metastasis, and the spinal canal are segmented. The necessary segmentations for *Step 1* were manually obtained by an image processing expert using a multi-label, live-wire approach. The vertebra was segmented in a CT scan, whereas the spinal canal and the metastasis were segmented in an MRI scan. These non-osseous structures were then transformed into the CT scan's coordinate system via rigid registration.

The general workflow of this step is simple: A pathway is defined in three orthogonal slice views via two points and is then visually assessed via the in-volume and on-mesh methods. They are intended to be used iteratively and we propose to begin the assessment with the in-volume method for two reasons: First, it indirectly depicts multiple pathways and their surroundings, thus the process of finding a pathway can be sped up. Secondly, the assessment of safety margins is temporarily more important than the final instrument placement.

For the in-volume Visualization, the pathway is transformed into a cylinder and from the corresponding voxels a 3D distance field is created. To create this distance field, first, all segmentation masks of risk structures are merged. Subsequently, for each voxel of the cylindrical

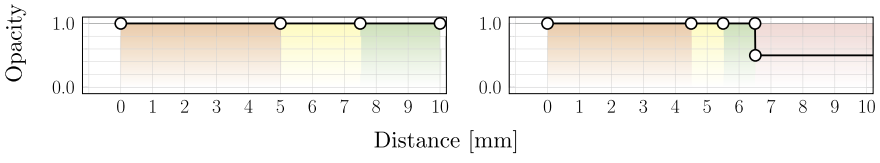

Fig. 2. Here, two exemplary in-volume (left) and on-mesh (right) transfer functions and their respective key points are depicted. The x-axes show distance values in mm, whereas the y-axes show the opacities for the key point color-coding.

Fig. 3. Experimental drilling setup: A *Mark-10 Force Test Stand ESM301* equipped with a *Mark-10 M5-20 Force Gauge* and custom-made drill.

volume, the absolute, minimum, and unsigned Euclidean distance to the combined risk structure mask is computed. In this context the spinal canal is the only risk structure, however, the method also works with combinations of multiple masks. Similar to Tappenbeck et al. [14], a transfer function (see Fig. 2) is used to map distance values to colors and opacities. A categorical green-yellow-red color scale is used to assist the process of distinct, clinical decision making. Various parameters are used to define four transfer function key points and default values are listed in Table 2. However, they can be changed interactively. For volume rendering, the cylinder is cut out from all segmentation masks, which creates a virtual pathway into the metastasis (see Fig. 5). Finally, the transfer function is applied to the 3D distance field.

The on-mesh visualization enables users to correct pathways with respect to osseous structures and to adapt the insertion depth. First, segmentations are transformed into vertex meshes. Then, the absolute, minimum, and unsigned Euclidean distance between each vertex and pathway sample point is computed. For the final color-coding (see Fig. 4), a different transfer function is used (cf. Tab. and Fig. 2), while the pathway is also represented by a gray applicator.

3.2. Step 2 – force estimation

Supervised by our clinical colleagues, drilling experiments for ten lumbar and five thoracic vertebrae were conducted. Since we had no access to fresh bones, fat freed and dried (conserved) vertebrae were used. Furthermore, no vertebra had anatomic abnormalities because of metastases. Before and after drilling, DynaCT scans were acquired: The acquisition time was set to 10 s and the voxels have an isotropic size of 0.46 mm. Using DynaCT instead of CT scans does not affect the validity of the presented results.

Fig. 3 shows the experimental setup for the drilling experiments and the drilling parameters are listed in Table 3. The setup consists of a *Mark-10 Force Test Stand ESM301*, which was programmed to move a *Mark-10 M5-20 Force Gauge* at a constant velocity of 2 mm/s. A custom-made drilling machine with a hollow drill was attached to the force gauge. The drilling machine was specified according to the *Arrow On-Control Byopsy System*, which is used by our clinical colleagues. Given the aforementioned voxel size, the used measurement frequency resulted in 230 force measurements per voxel. To stay in the optimal measuring range, we reduced the feed rate to 1 mm/s while drilling through the cortical bone.

To estimate drilling forces from image intensities, the drilling hole voxels have to be analyzed. First, a seed point for a 3D region growing is defined in the drilling hole of the post-drilling DynaCT scan. This results in a segmentation mask with over-segmentation artifacts, however, most voxels belong to the drilling hole. Subsequently, a Principal Component Analysis (PCA) on this segmentation mask is performed and the eigenvector corresponding to the largest eigenvalue represents the drilling path. Then, using the drill's outer diameter, a cylindrical segmentation mask is defined along this eigenvector, which is then used to obtain image intensities of bone tissue in the pre-drilling scan. The subsequent analysis of the masked image intensities is described in Section 4.1. Instead of this reconstruction, a pathway from Step 1 can be used.

4. Results

The aforementioned visualization methods were applied to scans of two cases. In the following figures, gray applicators represent the actual trajectories of cannulated trocars, which were reconstructed manually from intra-operative DynaCT scans.

Case 1. A 75-year-old male with kidney cancer on the left side presented himself with partial paralysis of his left leg, lower back pain, and forwarded leg pain. MRI scans showed a suspicious region in the fifth lumbar vertebra and its left pedicle. Furthermore, they showed hypointense image intensities and an increased contrast agent uptake. With an interdisciplinary team (*Tumor Board*) and the patient it was jointly decided to perform an RFA with a subsequent radiation therapy.

Here, the on-mesh method was used with an according transfer

Table 2
Listing of the parameters (upper table) and equations (lower table) used to construct the transfer function key points for the visualization methods. Some parameters were abbreviated: *HR* and *LR* for the high risk and low risk thresholds, *SO* and *RO* for the structure and risk visualization opacities, and *D* for the instrument's diameter.

Count	Name	Abbreviation	Visualization Method	Default Values
3	Risk Colors		in-volume & on-mesh	red, yellow, and green
1	Structure Color		on-mesh	red, yellow, and blue
2	Risk Thresholds	*HR* & *LR*	in-volume & on-mesh	5/ 10 mm or 1/ 3 mm
2	Opacity Values	*SO* & *RO*	in-volume & on-mesh	0.5 and 1
1	Instrument Diameter	*D*	on-mesh	1.5 mm

Method	Transfer Function Key Point Equations					
in-volume	$(0,\ 1)$	$(HR,\ 1)$	$\left(\frac{HR+LR}{2},\ 1\right)$	$(LR,\ 1)$		
on-mesh	$(0,\ RO)$	$\left(HR+\frac{D}{2},\ RO\right)$	$\left(\frac{HR+LR+D}{2},\ RO\right)$	$\left(LR+\frac{D}{2},\ RO\right)$	$\left(LR+\frac{D}{2}+\varepsilon,\ RO\right)$	$(maxDistance,\ SO)$

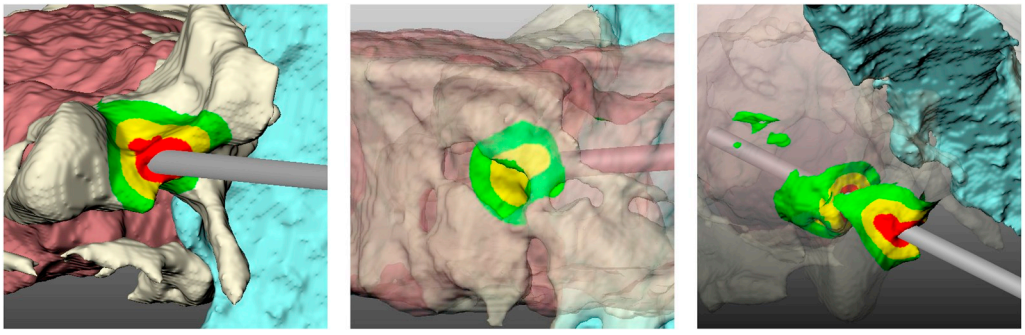

Fig. 4. The on-mesh visualization results for *Case 1*. The transpedicularly inserted, cannulated trocar, which is represented as a gray cylinder, was manually reconstructed from an intra-operative DynaCT scan. For the color-coding, the high and low risk thresholds were set to 1 and 3 mm, respectively. For the middle sub-figure, the color-coded surface mesh shows safety margins in ventral directions. Furthermore, for the rightmost sub-figure the opacities of the vertebra and metastasis surfaces were decreased to enable an simultaneous evaluation of the instrument's position and safety margins.

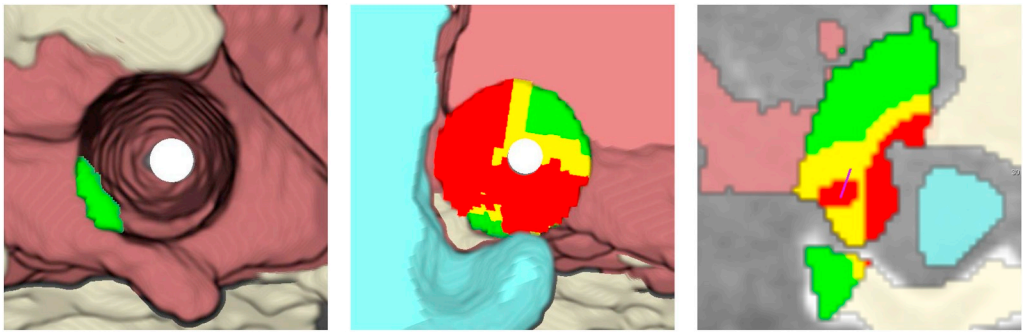

Fig. 5. The in-volume visualization result for *Case 2*. The left and middle sub-figures show detailed views of a Direct Volume Rendering of the remaining vertebra (brown), the metastasis (red), and spinal canal (blue), with a color-coded distance field cylinder. The sub-figures show the actual pathway of the inserted instruments (left) and a pathway that was deliberately placed in close proximity to the spinal canal in 3D (middle) and 2D (right). The stair-like color-coding in red is a result of a spinal cord compression in bottom-left direction of the pathway. Therefore, the pathway should be corrected in top-right direction.

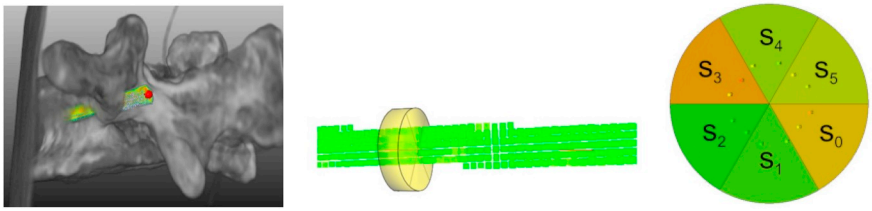

Fig. 6. The left sub-figure shows the virtual drilling path with respect to a volume rendered lumbar vertebra. The middle sub-figure shows a section of the virtual path without an anatomical context, but with a highlighted cross-section. Details about this cross-section are depicted in the right sub-figure: Each cross-section is partitioned into six segments. For each segment, a color-coding is applied according to the average HU using a green-to-red color scale: Green depicts small average values, whereas red depicts high average values.

Table 3
The drilling parameters for the vertebrae drilling experiments. The *Velocity* was lowered while drilling through cortical bone. A hollow drill was used, thus the column *Drill Diameters* states the respective inner and outer diameter.

Parameter	Velocity	Measurement Frequency	Drill Diameters	Nominal Speed	Nominal Torque
Value	1mm/s2mm/s	1 kHz	2mm3mm	420R/min	1.75Nm

function (see Fig. 2) and the results are provided in Fig. 4. The left sub-figure depicts how the instrument was inserted through the pedicle. For the middle sub-figure, color-coded safety margins were also applied to the metastasis' surface mesh, because it makes up the majority of the vertebra's front side. Therefore, the insertion depth is implicitly visualized, which makes it able to conclude about safety margins in ventral direction. The high and low risk thresholds were set to 1 and 3 mm, respectively, thus the color-coding intervals are as follows: Red from 0 mm to 2.5 mm, Yellow from 2.5 mm to 3.5 mm, and Green from 3.5 mm to 4.5 mm (cf. Table 2).

Case 2. A 59-year-old male with recurrent kidney cancer on the right side, liver and adrenal gland metastases, presented himself with lower back pain and adduction pain in the right hip. MRI scans revealed a suspicious region in the first lumbar vertebra and its right pedicle. They also revealed an increased contrast agent uptake, and he was at a high risk of spinal cord compression. It was jointly decided to perform an RFA the next day.

Here, the on-mesh method was used with an according transfer function (see Fig. 2) and the results can be seen in Fig. 5. The left sub-figure depicts the pathway of the cannulated trocar, which was inserted during intervention. The spinal canal was set to be the risk structure with $HR = 5$ mm and $LR = 10$ mm (cf. Table 2) and thus, the color-coding intervals are as follows: Red from 0 mm to 5 mm, Yellow from 5 mm to 7.5 mm, and Green from 7.5 mm to 10 mm. The cylinder's diameter, which is cut from all segmentation masks, was set to 10 mm. The reconstructed pathway did not show anything suspicious. Therefore, for the middle sub-figure, a second pathway was deliberately placed in close proximity to the spinal canal. Here, the main advantage of the in-volume method can be seen: As each distance field voxel represents the absolute, minimum distance between *this* voxel and all risk structure segmentation masks, the applied color-coding depicts safety margins in all spatial directions simultaneously. Therefore, because of the patient's beginning spinal cord compression, the in-volume method directly suggests a pathway correction in top right direction.

4.1. Verifying forces by comparing measured forces with image intensities

The future goal of this method is to verify a drill's position during robot-assisted bone drilling. Therefore, the relationship between HUs and drilling forces is analyzed. However, this relationship is not yet entirely understood. In contrast, there exist methods that approximate bone density from breaking tests, e. g., for hens [15]. We presented our earlier results when comparing drilling forces and intensity changes along drilling pathways [13]. There, we followed the notion that highly dense bone tissue directly results in increased drilling forces, i. e., local HU maxima near equidistant drilling path sample points. However, this resulted in unsystematic and false predictions. Therefore, highly dense bone tissue is not the only necessity for high drilling forces. Subsequently, averaged HUs were analyzed, which addressed false predictions only partially.

Upon analyzing the HU distribution around each sample point in a higher granularity, we could derive a more advanced method: After defining a cylindrical cross section around each sample point, each cross section is divided into six evenly shaped segments (see Fig. 6) and for each segment the average image intensity was computed. We assumed that structural integrity, which the drill has to work against, is not solely defined by a small, isolated slab of bone tissue or scan voxels and thus, larger areas of bone tissue should be considered. Therefore, the cross section's thickness was set to be three times the voxel spacing (1.4 mm) in drilling direction. Subsequently, we defined a *stiffness criterion* via discretization: A segment SE of a sample point SP is considered *stiff* if its average HU μ_{SE} is

$$\mu_{SE} > 0.8 \cdot IS_{max}$$

with IS_{max} being the largest HU within the vertebra's spongiosa. Note that in a scan the spongiosa of dried and fat-freed vertebrae contains air voxels. Although they have no relevance for the vertebrae's stiffness, they are included in a segmented drilling path. Therefore, an additional lower threshold for μ_{SE} was defined via

$$\mu_{SE} < 0.1 \cdot IS_{max}$$

to address bone tissue areas with no structural relevance. Finally, the following stiffness criterion ρ_{SP} was used to determine whether a sample point exhibit elevated stiffness:

$$\rho_{SP} = \begin{cases} 1, & \text{if } \forall\, \mu_{SE} > 0.1 \cdot IS_{max} \wedge \left(\sum^{\#SE} \mu_{SE} > 0.8 \cdot IS_{max}\right) \geq 3 \\ 0 & \text{else} \end{cases}$$

The blue curve in Fig. 7 shows the result when the stiffness criterion ρ_{SP} was applied: A sample point is considered stiff if none of its segments contains a lot of air, and at least half of all segments contain very dense bone tissue. If the criterion is fulfilled, increased drilling forces are required to maintain the current velocity. The systematic misalignment between both graphs is a result of having to drill through an uneven area on the corticalis. Therefore, we decreased the velocity there. However, using this criterion enabled us to predict high drilling force changes from HUs with an inaccuracy of less than ± 1 mm. Using this stiffness criterion still follows the notion that denser bone tissue requires higher drilling forces, but considering multiple key values per sample point enables a more accurate prediction of drilling force changes.

5. Evaluation

To evaluate the visualization methods, two neuroradiologists (I1 and I2, see Table 4) were interviewed informally using interactive questionnaires. One of them is a co-author of this submission. The interview setup was as follows: First, the interviewees were explained the general structure of the interview questionnaire and how to handle interactive elements, i. e., surface model rendering views, checkboxes, and text fields. For the interactive rendering views, it was explained

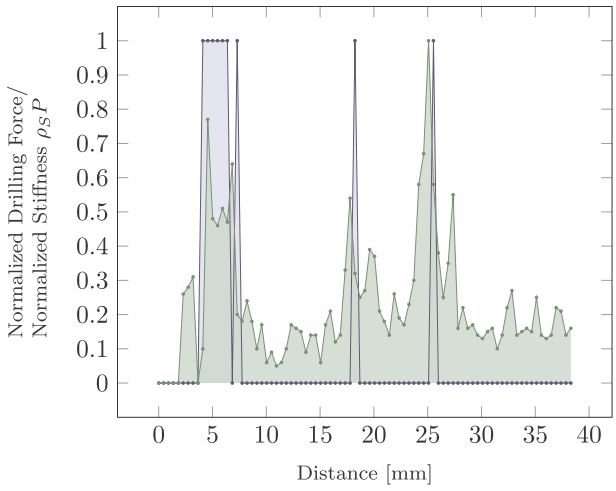

Fig. 7. Measured drilling forces (green) compared with the sample points' stiffness ρ_{SP} (blue) along the drilling path. Using the stiffness criterion from Section 4.1 enabled us to predict drilling force changes in a range of less than ± 1 mm.

Table 4
Results of the informal interview via interactive questionnaires. The upper part shows information about the interviewees. The lower part shows their answers with respect to presented visualization results (cf. Figs. 4 and 5).

	Interviewees	
	I1	I2
Gender	m	m
Age	49	29
Experience with planning and performing RFAs (yrs.)	12	4

Visualization Method	on-mesh				in-volume			
Case	C1		C2		C1		C2	
Interviewee	I1	I2	I1	I2	I1	I2	I1	I2
QE	++	+	++	+	+	+	+	+
QT	++	−−	+	−−				
QC					o	+	+	+
QIP	+	++	+	+	+	++	+	+
QIE	+	++	+	+	o	++	+	o
QIV	o	++	o	o	o	++	+	+
QMU	+	+	+	+	+	++	+	++

Legend: −− | − | o | + | ++

how to perform basic interactions, i. e., rotations, translations, and zooming. There were two rendering views, one for each Case (C1 and C2) and thus, the interviewees could explore case-individual 3D scenes with surface meshes of the segmented spinal canal, metastasis, and partially destroyed vertebra. Subsequently, used visualization parameters, such as used safety margins and opacity values (see Table 2), and respective visualization results (cf. Figs. 4 and 5) were presented for both cases after the on-mesh and in-volume methods were applied. To answer questions, the interviewees used a five-point Likert scale, including a neutral answer (− −, −, o, +, + +).

For each Case and visualization method, the interviewees were asked the following questions:

QE How easy-to-understand is the respective visualization method?

QT How sensible and useful do you rate the usage of transparencies to look into structures (on-mesh only)?

QC How sensible and useful do you rate the three-dimensional

encoding of the correction direction (in-volume only)?

Furthermore, they were asked to assess the usefulness of each visualization method regarding intervention planning (QIP), execution (QIE), and validation (QIV) of spinal RFAs and how likely they think it is that they would actually use the presented method (QMU).

The respective answers can be found in the lower part of Table 4, in which they are color-coded using a diverging red-gray-blue color-scale. Both interviewees considered the visualization methods to be easy-to-understand. However, their opinions differ regarding the usefulness of transparently presented surface meshes and three-dimensional color-coding of safety margins. Interviewee I1 considers transparencies beneficial (see Fig. 4), because they enable visual assessment of the instrument's orientation within the vertebra and metastasis and thus, it is easier to correct the instrument's placement, whereas interviewee I2 reported that colored and transparent surfaces did not provide any benefits for him. In contrast, I2 reported that the in-volume method (see Fig. 5), when compared to conventional two-dimensional presentations, to be superior, because distances between the currently selected drilling path and risk structures are visually encoded in all directions at once. However, interviewee I1 argued that the in-volume method produces visually complex results, which require around five to 10 min to be interpreted. Both experts agreed that both methods would be beneficial for intervention planning and execution of RFAs. However, this has to be validated in an extended evaluation in a clinical setting. For intervention validation, the assessment of necrotic bone tissue with respect to eventually remaining metastatic tissue is more important.

6. Discussion

The evaluation results show that our methods are feasible for their intended purpose, however, both experts agreed that their true usefulness has to be assessed in a real clinical setting. Interviewee I2 noted that they could also be used in an educational context, such as student seminars. However, both interviewees argued that obtaining patient-specific data for every intervention is too time-consuming and thus, an integration of (semi-)automatic segmentation and registration algorithms would be valuable additions to the presented approach. For example, Rak et al. published a survey article on spine analysis methods, including the localization, segmentation, and extraction of vertebrae and the spinal canal [16]. They also discuss automated methods for these tasks, however, we are not aware of automated segmentation methods for spinal metastases. The majority of automated methods either focus on brain tumors in MRI [17] or hepatic metastases in CT [18].

We argue that the slice-based search, assessment, and correction of feasible pathways is troublesome and time-consuming, because it is a spatially complex task, which requires neuroradiologists to iteratively examine and compare three-dimensional safety margins in one or multiple 2D views. This challenge is depicted in Fig. 5: If the pathway for the middle and right sub-figure is examined in 2D, the pathway would be corrected in lateral direction, although it would still be too close in inferior direction. In contrast, using the in-volume method directly proposes a correction in top-right direction, which safes one additional correction. Both interviewed experts acknowledged our methods' potential, however, this assumption has to be evaluated thoroughly. Given that safety margins, the insertion depth, and instrument's diameter are important risk aspects for various needle-based operations and interventions, the presented two-step method could also be applicable in a different setting.

There exist approaches that aim to offer robot-assistance during spine interventions [19]. The proposed method could be tested in such settings, for example, by comparing a pre-interventionally estimated drilling force profile and intra-interventionally measured drilling forces, via a robot-mounted force gauge (cf. Fig. 3). In addition to the robot's ability to augment its operator's movements with tremor-free, scaled, and constraint motions, the presented stiffness criterion could be used to validate the drill's position with respect to insertion depth and both drilling profiles. If both profiles are too different, e. g., a predicted increase in required drilling forces occurs too soon or late, the robot fixes its position and signals its operator to examine the situation, because the drill could be guided along a different pathway. Depending on the situation, an additional scan can be acquired to evaluate the drill's current position inside the patient using the visualization methods of Step 1. Manually conducted interventions can also be assisted. However, instruments with ruler marks and tracking facilities have to be used to validate insertion depth and angle, respectively.

For the current analysis, pre- and post-operative images of conserved vertebrae were analyzed. The presented results confirm the hypothesis that image intensities and force changes are correlated. It can be expected that the physical properties of bones change significantly during conservation and that more force is required to drill through fresh bone tissue [15]. However, there exists no data that describes how these properties change during conservation. Therefore, we are planning further drilling experiments with ex-vivo and conserved vertebrae to analyze these property changes. This analysis is necessary to validate if conserved vertebrae can be used to reliably predict drilling forces for fresh bones, or if fresh bones have to be used. However, the segmentation and analysis methods have to be refined, because more image artifacts are expected, e. g. because of blood vessels inside the spongiosa.

If the drill is not inserted perpendicular to the bone's corticalis, it is challenging to align the force and image intensity curves. First, it was assumed that with respect to the drilling path the corticalis could be used to align both curves, because of the first large increase of drilling forces. However, inserting the drill at a more shallow angle results in an unexpected slow increase of drilling forces. During intervention, it is reasonable that physicians specify the moment of contact between instrument and bone surface manually. Therefore, it is also evaluated if a manual alignment is feasible, too.

Currently, the visualization results of the first step are not updated in real-time when the pathway is adapted. Regarding the on-mesh method, using an i5-2500 CPU with 3.30 GHz and a pathway with 2500 sample points results in approximately 0.9s per 100000 surface mesh patches. This can be improved by decreasing the number of sample points and mesh patches and parallel processing. Regarding the in-volume method, it takes less than 18s to process approximately 14.5 million voxels. However, once risk and non-risk structures are separated, the distance field generation has to be done only once. Thus, performance benefits might be marginal.

7. Conclusion and outlook

In this work, a two-step method was presented that intends to improve intervention planning and execution of spine RFAs. The method aims at cognitive assistance via 3D visualizations of chosen risk aspects, and could offer physical assistance in the future during robot-assisted interventions.

An informal evaluation showed that the visualization methods of Step 1 enable an easy assessment of safety margins, spatial relationships between anatomic structures, and drilling paths. If all prerequisites are met, they could potentially speed up the pathway finding process, however, this assumption has to be evaluated thoroughly in the future. Additionally, a study that evaluates and compares various risk aspects with respect to their clinical application scenarios is very desirable. Moreover, research about how different types of metastases, RFA electrode positioning, varying electrode currents, coagulated tissue, and remaining metastatic bone tissue relate to each other is urgently needed.

Bone drilling is a challenging task. The presented stiffness criterion is another step to better understand the relationship between image intensities and drilling forces. The presented stiffness criterion could be

used for robot-assisted interventions in the future to validate the positioning of drills with respect to previously defined drilling force profiles and currently measured drilling forces. The presented parameters were found by observations alone. Further investigations are required to optimize them, for example, via machine based learning.

Ethic statement

For this type of study formal consent is not required.

Conflicts of interest

The authors declare that they have no conflict of interest.

Acknowledgments

This work is partly funded by the Federal Ministry of Education and Research within the Forschungscampus *STIMULATE* (13GW0095A, 13GW0095B). Furthermore, we want to thank Karin Fischer for sharing her anatomical knowledge and Steffen Serowy for his technical support. Finally, we want to thank Oliver Beuing for being our second interviewee.

References

[1] R. Coleman, J.-J. Body, M. Aapro, P. Hadji, J. Herrstedt, Bone health in cancer patients: ESMO clinical practice guidelines, Ann. Oncol. 25 (suppl_3) (2014), https://doi.org/10.1093/annonc/mdu103 iii124–iii137.

[2] A.N. Gazis, O. Beuing, J. Franke, B. Jöllenbeck, M. Skalej, Bipolar radiofrequency cblation of spinal tumors: predictability, safety and outcome, Spine J. 14 (4) (2014) 604–608, https://doi.org/10.1016/j.spinee.2013.06.081.

[3] C. Baegert, C. Villard, P. Schreck, L. Soler, Multi-criteria trajectory planning for hepatic radiofrequency ablation, Proc. Of Medical Image Computing and Computer-Assisted Intervention (MICCAI), vol.4792, 2007, pp. 676–684, https://doi.org/10.1007/978-3-540-75759-7_82.

[4] G. Zombori, R. Rodionov, M. Nowell, M.A. Zuluaga, M.J. Clarkson, C. Micallef, B. Diehl, T. Wehner, A. Miserochi, A.W. McEvoy, J.S. Duncan, S. Ourselin, A computer assisted planning system for the placement of sEEG electrodes in the treatment of epilepsy, Proc. Of Information Processing in Computer-Assisted Interventions (IPCAI), vol.8498, 2014, pp. 118–127, https://doi.org/10.1007/978-3-319-07521-1_13.

[5] N.V. Navkar, N.V. Tsekos, J.R. Stafford, J.S. Weinberg, Z. Deng, Visualization and planning of neurosurgical interventions with straight access, Proc. Of Information Processing in Computer-Assisted Interventions (IPCAI), vol.6135, 2010, pp. 1–11, https://doi.org/10.1007/978-3-642-13711-2_1.

[6] M. Rincón-Nigro, N.V. Navkar, N.V. Tsekos, Z. Deng, GPU-accelerated interactive visualization and planning of neurosurgical interventions, IEEE COMPUT GRAPH 34 (1) (2014) 22–31, https://doi.org/10.1109/MCG.2013.35.

[7] P.-C. Herghelegiu, V. Manta, R. Perin, S. Bruckner, E. Gröller, Biopsy planner – visual analysis for needle pathway planning in deep seated brain tumor biopsy, Comput. Graph. Forum 31 (3pt2) (2012) 1085–1094, https://doi.org/10.1111/j.1467-8659.2012.03101.x.

[8] C. Rieder, A. Weihusen, C. Schumann, S. Zidowitz, H.-O. Peitgen, Visual support for interactive post-interventional assessment of radiofrequency ablation therapy, Comput. Graph. Forum 29 (3) (2010) 1093–1102, https://doi.org/10.1111/j.1467-8659.2009.01665.x.

[9] N.A. Ghanem, M. Uhl, I. Brink, O. Schäfer, T. Kelly, E.A. Moser, M.F.J. Langer, Diagnostic value of MRI in comparison to scintigraphy, PET, MS-CT and PET/CT for the detection of metastases of bone, Eur. J. Radiol. 55 (1) (2005) 41–55, https://doi.org/10.1016/j.ejrad.2005.01.016.

[10] T. Butz, S.K. Warfield, K. Tuncali, S.G. Silverman, E. van Sonnenberg, F.A. Jolesz, R. Kikinis, Pre-and intra-operative planning and simulation of percutaneous tumor ablation, Proc. Of Medical Image Computing and Computer-Assisted Intervention (MICCAI), vol.1935, 2000, pp. 317–326, https://doi.org/10.1007/978-3-540-40899-4_32.

[11] A. Littmann, A. Schenk, B. Preim, G. Prause, K. Lehmann, A. Roggan, H.-O. Peitgen, Planning of anatomical resections and in-situ ablations in oncologic liver surgery, Proc. Of Computer Assisted Radiology and Surgery (CARS), vol.1256, 2003, pp. 684–689, https://doi.org/10.1016/S0531-5131(03)00319-4.

[12] F. Ritter, T. Boskamp, A. Homeyer, H. Laue, M. Schwier, F. Link, H.-O. Peitgen, Medical image analysis, IEEE PULSE 2 (6) (2011) 60–70, https://doi.org/10.1109/MPUL.2011.942929.

[13] N. Merten, S. Adler, M. Hanses, S. Saalfeld, M. Becker, B. Preim, Two-step trajectory visualization for robot-assisted spine radiofrequency ablations, Proc. of Workshop Bildverarbeitung für die Medizin (BVM), 2018, pp. 55–60, https://doi.org/10.1007/978-3-662-56537-7_29.

[14] A. Tappenbeck, B. Preim, V. Dicken, Distanzabhängige Transferfunktionen für die medizinische Volumenvisualisierung, Proc. of Workshop Bildverarbeitung für die Medizin (BVM), 2005, pp. 307–311, https://doi.org/10.1007/3-540-26431-0_63.

[15] W.K. Kim, L.M. Donalson, P. Herrera, C.L. Woodward, L.F. Kubena, D.J. Nisbet, S.C. Ricke, Research note: effects of different bone preparation methods (fresh, dry, and fat-free dry) on bone parameters and the correlations between bone breaking strength and the other bone parameters, Poultry Sci. 83 (10) (2004) 1663–1666, https://doi.org/10.1093/ps/83.10.1663.

[16] M. Rak, K.-D. Tönnies, On computerized methods for spine analysis in MRI: a systematic review, INT J COMPUT ASS RAD 11 (8) (2016) 1445–1465, https://doi.org/10.1007/s11548-016-1350-2.

[17] J. Liu, M. Li, J. Wang, F. Wu, T. Liu, Y. Pan, A survey of MRI-based brain tumor segmentation methods, Tsinghua Sci. Technol. 19 (6) (2014) 578–595, https://doi.org/10.1109/TST.2014.6961028.

[18] J.H. Moltz, L. Bornemann, J.-M. Kuhnigk, V. Dicken, E. Peitgen, S. Meier, H. Bolte, M. Fabel, H.-C. Bauknecht, M. Hittinger, A. Kießling, M. Pusken, H.-O. Peitgen, Advanced segmentation techniques for lung nodules, liver metastases, and enlarged lymph nodes in CT scans, IEEE J SEL TOP SIGNA 3 (1) (2009) 122–134, https://doi.org/10.1109/JSTSP.2008.2011107.

[19] M. Hanses, S. Adler, S. Wolff, M. Skalej, N. Elkmann, Robotic assistance for spine interventions, Proc. Of German Society of Computer- and Robot-Assisted Surgery (CURAC), vol.15, 2016, pp. 231–236, https://doi.org/10.4126/FRL01-006401254.